DFT Studies of Dimethylaminophenyl-substituted Phthalocyanine and of Its Silver Complexes

Martin Breza *

Posted Date: 5 February 2024

doi: 10.20944/preprints202402.0251.v1

Keywords: B3LYP hybrid functional; solvent effect; geometry optimization; electron structure; spin density; electron transitions

Article

DFT Studies of Dimethylaminophenyl-Substituted Phthalocyanine and of Its Silver Complexes †

Martin Breza

Department of Physical Chemistry, Slovak Technical University, Radlinskeho 9, SK-81237 Bratislava, Slovakia; martin.breza@stuba.sk

† In the memory of Professor Stanislav Biskupič (1949-2016).

Abstract: The dimethylaminophenyl-substituted silver phthalocyanine [dmaphPcAg] can be used as a UV-vis photoinitiator for in situ preparation of a silver/polymer nanocomposite. To verify early steps of the supposed mechanism of radical polymerization, we performed quantum chemical calculations of ^{m}[dmaphPcAg]^{q} complexes with charges q = +1 to -2 in the two lowest spin states m, of a free ligand and its dehydrogenated/deprotonated products ^{m}[dmaphPcH$_n$]^{q}, n = 2 to 0, q= 0, -1 or -2, in the lowest spin states m. The calculated electronic structures and electron transitions of all the optimized structures in $CHCl_3$ solutions are compared with experimental EPR and UV-vis spectra, respectively. The unstable ^{3}[dmaphPcAg]$^{+}$ species deduced only from previous EPR spin trap experiments was identified. In addition to ^{2}[dmaphPcAg]^{0}, our results suggest the coexistence of both reaction intermediates ^{1}[dmaphPcAg]$^{-}$ and ^{3}[dmaphPcAg]$^{-}$ in reaction solutions. Silver nanoparticle formation is a weak point of the supposed reaction mechanism from the energetic, stereochemistry, and electronic structure points of view.

Keywords: B3LYP hybrid functional; solvent effect; geometry optimization; electron structure; spin density; electron transitions

1. Introduction

Phthalocyanine $(C_8H_4N_2)_4H_2$ (PcH_2) contains four isoindole units connected by nitrogen bridges. The so-obtained ring system has 18 delocalized π electrons responsible for intense absorption (the Soret band around 400 nm and the Q-band in the red/near infrared region). Therefore, phthalocyanines are used as dyes and pigments [1]. Metal complexes derived from Pc^{2-} have applications in catalysis, solar cells, and photodynamic therapy [1–17].

Very high absorption in the visible range and high chemical resistance implied the synthesis of complexes of various substituted phthalocyanines with central Al, Mg, and Zn atoms [18–22] to be used as photoinitiators for free-radical (FRP) and/or cationic (CP) polymerizations. Recently, Breloy et al. [23] have synthesized a complex of dimethylaminophenyl-substituted phthalocyanine with silver in an unusual oxidation state +II, [dmaphPcAg] (see Fig. 1). The species obtained by photoinduced electron transfer reactions of excited [dmaphPcAg]* in the presence and absence of bis(4-methylphenyl)iodonium hexafluorophosphate (Iod) initiated CP and FRP, respectively, both in laminate as well as under air. Moreover, a polymer/silver nanocomposite with a homogenous narrow size distribution of spherical silver nanoparticles has been formed.

 doi:10.20944/preprints202402.0251.v1

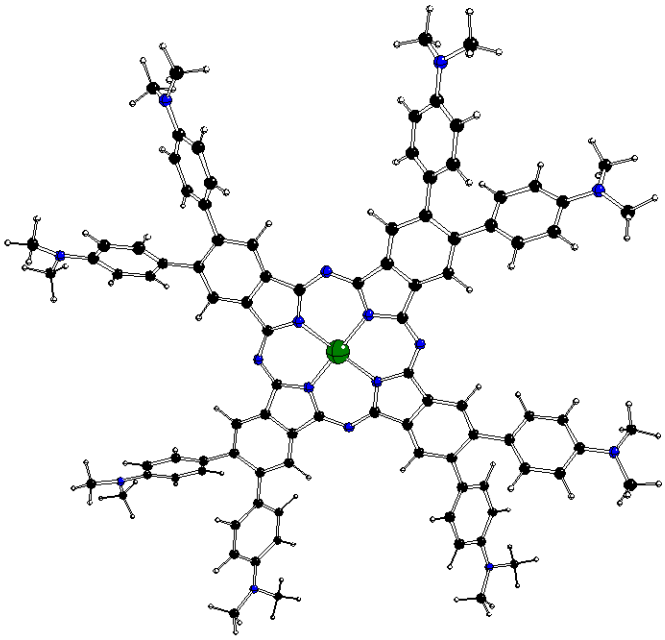

Figure 1. DFT optimized structure of ^{2}[dmaphPcAg]^{0} in $CHCl_3$ (C – black, N – blue, Ag – green, H – white) [23].

Our recent study will deal with the results related to [dmaphPcAg] and its reaction intermediates in more detail [23]. Its UV-vis absorption spectrum in $CHCl_3$ shows two intense absorption peaks at ca. 300 - 360 nm (Soret band) and at 700 nm (Q-band) (see Fig. 2). According to TD-B3LYP/SMD (see below) calculations of its neutral molecule in doublet ground spin state), ^{2}[dmaphPcAg]^{0}, the Soret band corresponds most probably to $\pi - \pi^*$ ligand-metal electron transitions at 359 nm (oscillator strength f = 0.76). The Q-band consists of $\pi - \pi^*$ electron transitions at 723 nm (f = 0.9) and at 724 nm (f = 0.79). Analogously, in the neutral dmaphPcH_2 molecule in singlet ground state (Fig. 3) the Soret band at ca 340 nm could be ascribed to $\pi - \pi^*$ electron transitions at 376 nm (f = 0.19) and at 404 nm (f = 0.23) and the Q-band at ca 740 nm is explained by $\pi - \pi^*$ electron transitions at 736 nm (f = 0.82) and at 713 nm (f = 0.22).

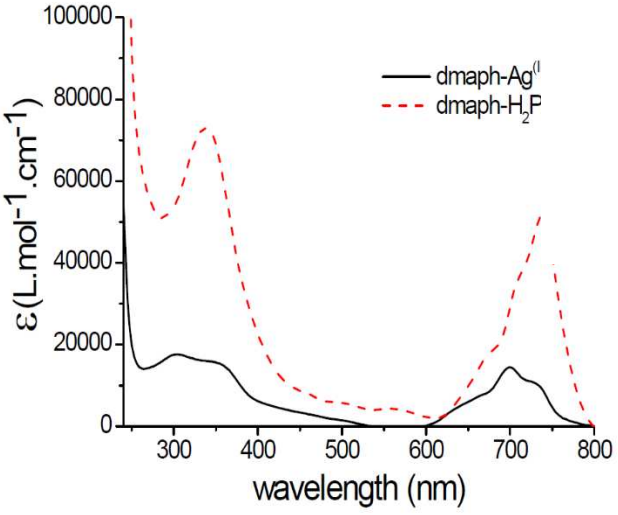

Figure 2. UV-vis spectra of neutral dmaphPcAg (full line) and dmaphPcH_2 (dashed line) in $CHCl_3$ [23].

 doi:10.20944/preprints202402.0251.v1

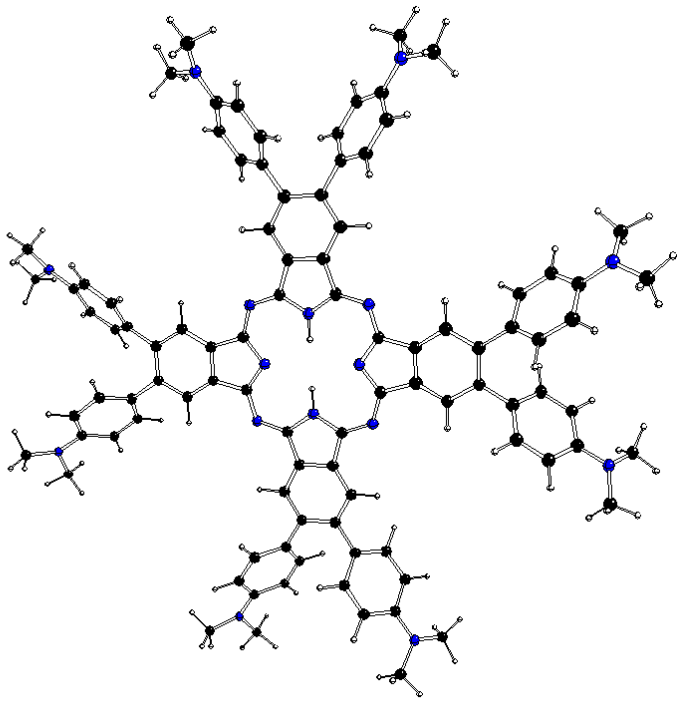

Figure 3. DFT optimized structure of $^{1}[dmaphPcH_2]^{0}$ in $CHCl_3$ (C – black, N – blue, H – white).

Under exposure to LED @ 385 nm of [dmaphPcAg] in $CHCl_3$ solutions with and without Iod, a sharp decrease in absorbance at 359 and 723 nm is observed simultaneously with splitting the Q-band and a rapid increase in a band at 450 nm indicating the formation of silver nanoparticles (see Fig. 4) [23]. Well-dispersed spherical Ag nanoparticles in the solution (an average diameter of 9 nm) were confirmed by transmission electron microscopy. Fluorescence quenching increases with Iod concentration in a chloroform solution, which suggests an electron transfer reaction from the [dmaphPcAg] excited state to Iod.

A very weak EPR signal of in situ irradiated [dmaphPcAg] in $CHCl_3$ using LED@385 nm was detected at g = 2.0021 and its intensity was enhanced in the presence of Iod [23]. It can be assigned to an unstable π-radical cation which is probably transformed into a N-centered radical that was detected as an adduct with N-benzylidene-tert-butylamine N-oxide (PBN) or 2,2-dimethyl-3,4-dihydro-2H-pyrrole 1-oxide (DMPO). The carbon- and nitrogen-centered radicals were detected in similar EPR experiments with PBN and DMPO spin-traps in deoxygenated benzene under argon as well.

Preprints.org (www.preprints.org) | NOT PEER-REVIEWED | Posted: 5 February 2024 doi:10.20944/preprints202402.0251.v1

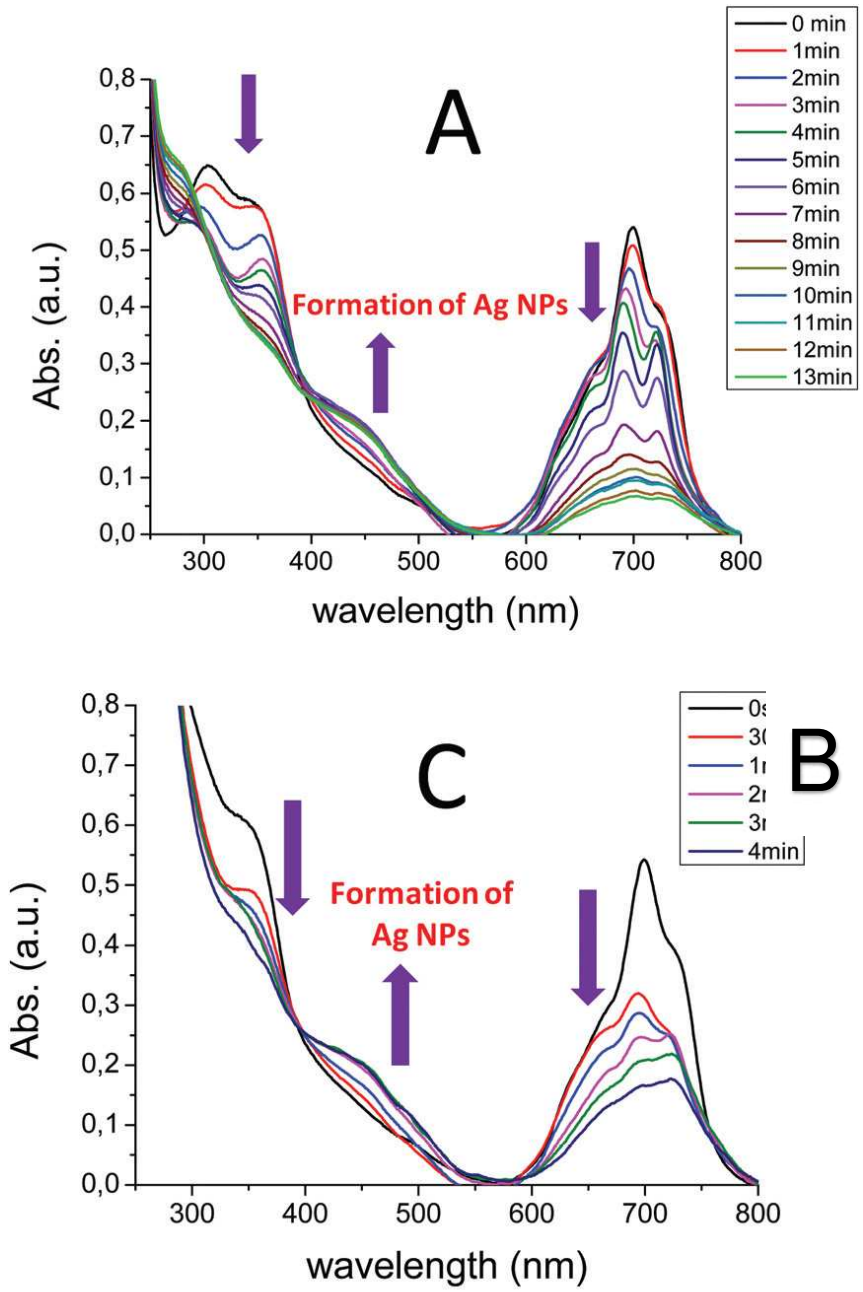

Figure 4. Time dependence of absorption spectra during photolysis of (A) $[dmaphPcAg]^0$ and (B) $[dmaphPcAg]^0$/Iod under LED@385 nm irradiation. LED@385 nm intensity = 470 mW cm^{-2}. Concentration of Iod = 7.9×10^{-5} M, concentration of $[dmaphPcAg]^0$ = 3.8×10^{-5} M. Solvent = $CHCl_3$ [23].

LED@385 nm irradiation of [dmaphPcAg] in $CHCl_3$ with Iod under argon formed a π-radical cation centered on [dmaphPcAg]. Stable (4-methyl)phenyl radical adducts with PBN, DMPO and nitrosodurene spin traps were detected in similar experiments in deoxygenated benzene under argon as well.

The Iod addition to [dmaphPcAg] photoinitiating systems caused higher conversions of epoxy and acrylate monomers [23]. Similar results can be obtained by cationic photopolymerization using the $dmaphPcH_2$/Iod system and $dmaphPcH_2$ alone. Therefore, the presence of Ag is not crucial for photopolymerization. Because radical species are strongly inhibited by oxygen, FRP does not proceed well in air. Unlike acrylate conversions, epoxy conversions are not affected by atmosphere conditions. Another interesting attribute of the above [dmaphPcAg] photoinitiating systems is the electron

 doi:10.20944/preprints202402.0251.v1

transfer reactions where the central Ag(II) atom is reduced to homogenously dispersed silver nanoparticles in the polymer matrix.

The following [dmaphPcAg] photoinitiation mechanism was proposed [23]:

The photoexcited [dmaphPcAg]* *is formed by irradiation in the first step*

$$[dmaphPcAg] + h\upsilon \rightarrow [dmaphPcAg]^* \quad (1)$$

The reaction between photoexcited and ground-state species leads to the reduction of Ag(II) to Ag(I) and generates the nitrogen-centered cation-radical in the second step

$$[dmaphPcAg]^* + [dmaphPcAg] \rightarrow [dmaphPcAg]^- + [dmaphPcAg]^{+\bullet} \quad (2)$$

In the third step, silver nanoparticles and aromatic carbon-centered radicals are formed.

$$[dmaphPcAg]^- \rightarrow Ag^0 + [dmaphPc]^{-\bullet} \quad (3)$$

Subsequently, a hydrogen-transfer reaction between $[dmaphPcAg]^{+\bullet}$ and [dmaphPcAg] leads to dehydrogenated aromatic-derived aminoalkyl radicals [dmaphPcAg - H]$^\bullet$ and Brønsted photoacids H^+ according to (4)

$$[dmaphPcAg]^{+\bullet} + [dmaphPcAg] \rightarrow [dmaphPcAg] + [dmaphPcAg - H]^\bullet + H^+ \quad (4)$$

The Brønsted acids subsequently initiate ring-opening reactions in epoxides. $[dmaphPc]^{-\bullet}$ and [dmaphPcAg - H]$^\bullet$ initiate the FRP of acrylates.

The addition to [dmaphPcAg] is the source of additional CP reactions. Upon irradiation, the exciplex $[dmaphPcAg\ldots(MePh)_2I^+]^*$ is formed

$$[dmaphPcAg] + (MePh)_2I^+ + h\upsilon \rightarrow [dmaphPcAg\ldots(MePh)_2I^+]^* \quad (5)$$

Subsequently, it undergoes electron transfer (6), where the $[dmaphPcAg]^{+\bullet}$ cation-radical and a diaryliodo radical are formed

$$[dmaphPcAg\ldots(MePh)_2I^+]^* \rightarrow [dmaphPcAg]^{+\bullet} + (MePh)_2I^\bullet \quad (6)$$

Similar electron transfer reactions as above within [dmaphPcAg]* cause the formation of silver nanoparticles, $[dmaphPc]^{-\bullet}$, [dmaphPcAg-H]$^\bullet$, and photoacids - see Eqs. (2) – (4). The intermediate diaryliodo radical is unstable and decomposes as follows

$$(MePh)_2I^\bullet \rightarrow MePh^\bullet + MePhI \quad (7)$$

So formed phenyl radicals can abstract hydrogen and produce the derived aromatic aminoalkyl radical [dmaphPcAg-H]$^\bullet$

$$[dmaphPcAg] + MePh^\bullet \rightarrow [dmaphPcAg\text{-}H]^\bullet + MePhH \quad (8)$$

The generated $[dmaphPc]^{-\bullet}$ and [dmaphPcAg-H]$^\bullet$ radicals are able to initiate the FRP of acrylates.

Nevertheless, the above reaction mechanism (1) – (8) meets several problems. Whereas [dmaphPcAg], [dmaphPcAg]* and $[dmaphPcAg\ldots(MePh)_2I^+]^*$ have an odd number of electrons and their doublet ground spin state corresponds to natural radicals, $[dmaphPcAg]^-$, $[dmaphPcAg]^+$, and the monodehydrogenated species [dmaphPcAg - H] have an even number of electrons and so they can form biradicals. These correspond to singlet or triplet spin states, but the singlet biradicals are not detectable by EPR measurements. Consequently, quantum-chemical calculations are necessary to describe their spin densities. In [23] quantum-chemical calculations of neutral [dmaphPcAg] in doublet spin state and neutral $[dmaphPcH_2]$ in singlet spin state were performed only. In our more recent (TD-)B3LYP study [24] optimal geometries, electronic structure and electron transitions of $^m[dmaphPcAg]^q$ species in vacuum with charges q = +1 to -2 in the two lowest spin states m were investigated from the point of view of the Jahn-Teller effect. However, this study was not related to spin distribution in the $^m[dmaphPcAg]^q$ species.

The aim of our recent manuscript is to complete the previous studies by DFT calculations of $^m[dmaphPcAg]^q$ species in $CHCl_3$ with various charges q corresponding to silver oxidation states

 doi:10.20944/preprints202402.0251.v1

between +III and 0 and in two lowest spin states m. We want to describe their electron- and spin-density distributions. To complete the picture, we will also study the dehydrogenated/deprotonated ^{1}[dmaphPcH$_2$]^0 species in the lowest spin states. We hope that the obtained results on electronic structure, energetics and electron transitions will contribute to verification of the above mentioned reaction mechanism (1) – (3) [23].

2. Results

Geometry optimization of ^{m}[dmaphPcAg]^q complexes in $CHCl_3$ in two lowest spin states without any symmetry restriction (see below) started from their optimized structures in vacuum obtained in [24]. After suitable modifications, these structures were used as starting ones for analogous geometry optimizations of dehydrogenated/deprotonated species [dmaphPcH$_2$] in the lowest two spin states as well. Although the singlet spin states of the systems under study were treated using an unrestricted formalism (the 'broken symmetry' treatment [25]), no spin-polarized solutions were obtained, i.e., their energies are identical as in the case of restricted DFT calculations. Gibbs free energies and relevant geometry parameters of the stable structures are presented in Tables 1 - 3.

Table 1. Absolute (G_{298}) and relative (ΔG_{298}) Gibbs free energies at 298 K of ^{m}[dmaphPcAg]^q and ^{m}[dmaphPcH$_n$]^0 species in $CHCl_3$ under study, n = 2→0, in various charge (q) and spin (m) states.

Compound	q	m	G_{298} [Hartree]	ΔG_{298} [kJ/mol]
^{1}[dmaphPcAg]$^{+}$	+1	1	-4733.24222	453.4
^{3}[dmaphPcAg]$^{+}$	+1	3	-4733.25119	429.9
^{2}[dmaphPcAg]^{0}	0	2	-4733.41492	0.0
^{4}[dmaphPcAg]^{0}	0	4	-4733.38011	91.4
^{1}[dmaphPcAg]$^{-}$	-1	1	-4733.51744	-269.2
^{3}[dmaphPcAg]$^{-}$	-1	3	-4733.51527	-263.5
^{2}[dmaphPcAg]$^{2-}$	-2	2	-4733.59008	-459.9
^{4}[dmaphPcAg]$^{2-}$	-2	4	-4733.57970	-432.6
^{1}[dmaphPcH$_2$]^0	0	1	-4587.58495	0.0
^{1}[dmaphPcH]$^{-}$	-1	1	-4587.08582	1310.5
^{2}[dmaphPcH]^0	0	2	-4586.94941	1668.6
^{1}[dmaphPc]$^{2-}$	-2	1	-4586.54403	2732.9
^{2}[dmaphPc]$^{-}$	-1	2	-4586.43712	3013.6

Table 2. Relevant geometric and electronic structure parameters of the ^{m}[dmaphPcAg]^q systems in $CHCl_3$ (see Table 1) related to the central Ag, pyrrole N_{py}, bridging N_{br}, aminyl N_{amin}, methyl C_{met} and isoindole C atoms in 4-, 7- (C_α) and 5-, 6- (C_β) positions (adj = adjacent, op = opposite bond angles).

q	+1	+1	0	0	-1	-1	-2	-2
m	1	3	2	4	1	3	2	4
Bond length [Å]								
Ag-N_{py}	2.000(4×)	2.056(4×)	2.059(4×)	2.058(2×) 2.062(2×)	2.067(2×) 2.133(2×)	2.063(2×) 2.067(2×)	2.072(4×)	2.071(4×)

 doi:10.20944/preprints202402.0251.v1

Ag – plane distance [Å]								
N_{py} plane	0.001	0.019	0.007	0.000	0.005	0.000	0.000	0.000
Bond angle [deg]								
$(N_{py}\text{-Ag-}N_{py})_{adj}$	90.0(4×)	90.0(4×)	90.0(4×)	90.0(4×)	89.9(2×) 90.1(2×)	90.0(4×)	90.0(4×)	90.0(4×)
$(N_{py}\text{-Ag-}N_{py})_{op}$	179.9(2×)	178.9(2×)	179.7(2×)	180.0(2×)	179.2 179.5	180.0(2×)	180.0(2×)	180.0(2×)
Bond order								
Ag-N_{py}	0.448(4×)	0.377(4×)	0.379(4×)	0.379(2×) 0.377(2×)	0.363(2×) 0.330(2×)	0.382(2×) 0.381(2×)	0.383(4×)	0.384(4×)
Charge								
Ag	1.023	0.857	0.843	0.833	0.713	0.814	0.787	0.785
N_{py}	-0.574(4×)	-0.623(4×)	-0.614(4×)	-0.613(2×) -0.662(2×)	-0.637(2×) -0.614(2×)	-0.603(2×) -0.647(2×)	-0.633(2×) -0.637(2×)	-0.634(4×)
N_{br}	-0.533(4×)	-0.553(4×)	-0.550(4×)	-0.587(4×)	-0.566(4×)	-0.579(4×)	-0.617(4×)	-0.610(4×)
C_{α}	0.497(8×)	0.528(8×)	0.485(8×)	0.484(4×) 0.532(4×)	0.464(4×) 0.435(4×)	0.422(4×) 0.476(4×)	0.422(8×)	0.418(8×)
C_{β}	-0.083(8×)	-0.092(8×)	-0.085(8×)	-0.101(4×) -0.086(4×)	-0.083(4×) -0.091(4×)	-0.100(4×) -0.081(4×)	-0.101(8×)	-0.101(8×)
N_{amin}	-0.482(8×)	-0.475(8×)	-0.492(8×)	-0.489(8×)	-0.497(8×)	-0.497(8×)	-0.502(8×)	-0.502(8×)
C_{met}	-0.418(16×)	-0.418(16×)	-0.418(16×)	-0.418(16×)	-0.418(16×)	-0.418(16×)	-0.418(16×)	-0.418(16×)
d electron population								
Ag	9.23	9.43	9.43	9.44	9.58	9.44	9.45	9.45
Spin population								
Ag	-	0.426	0.422	0.426	-	0.420	0.412	0.415
N_{py}	-	0.119(4×)	0.148(4×)	0.080(2×) 0.206(2×)	-	0.120(2×) 0.234(2×)	0.259(2×) 0.039(2×)	0.208(4×)
N_{br}	-	-0.037(4×)	0.002(4×)	0.009(4×)	-	0.054(4×)	-0.001(4×)	0.115(4×)
C_{α}	-	0.086(8×)	-0.007(8×)	0.237(4×) 0.100(4×)	-	0.104(4×) -0.016(4×)	-0.106(4×) 0.096(4×)	0.079(8×)
C_{β}	-	-0.007(8×)	0.006(8×)	0.016(4×) -0.002(4×)	-	0.037(4×) 0.004(4×)	-0.043(4×) 0.054(4×)	0.047(8×)
N_{amin}	-	0.016(8×)	0.000(8×)	0.005(8×)	-	0.000(8×)	0.000(8×)	0.001(4×)
C_{met}	-	-0.001(16×)	0.000(16×)	-0.000(16×)	-	0.000(16×)	0.000(16×)	0.000(16×)

 doi:10.20944/preprints202402.0251.v1

Table 3. Relevant geometric and electronic structure parameters of ^{m}[dmaphPcAg]^{q} systems in $CHCl_3$ (see Table 1) related to pyrrole N_{py}, bridging N_{br}, aminyl N_{amin}, methyl C_{met} and isoindole C atoms in 4-, 7- (C_{α}) and 5-, 6- (C_{β}) positions.

Compound	**^{1}[dmaphPcH$_2$]^{0}**	**^{1}[dmaphPcH]$^{-}$**	**^{2}[dmaphPcH]^{0}**	**^{1}[dmaphPc]$^{2-}$**	**^{2}[dmaphPc]$^{-}$**
q	0	-1	0	-2	-1
m	1	1	2	1	2
Bond length [Å]					
H-N_{py}	1.017(2×)	1.028	1.029	-	-
Bond order					
H-N_{py}	0.659(2×)	0.648	0.645	-	-
Charge					
N_{py}	-0.607(2×) -0.656(2×)	-0.577 -0.613 -0.615	-0.579 -0.617(2×) -0.628	-0.560(4×)	-0.566(4×)
N_{br}	-0.550(4×)	-0.611 -0.571(2×) -0.565(2×)	-0.566(2×) -0.571(2×)	-0.588(4×)	-0.592(4×)
C_{α}	0.488(4×) 0.475(4×)	0.461(2×) 0.462(4×) 0.450(2×)	0.513(2×) 0.519(2×) 0.510(2×) 0.529(2×)	0.434(8×)	0.500(8×)
C_{β}	-0.084(4×) -0.090(4×)	-0.087(2×) -0.085(4×) -0.092(2×)	-0.094(2×) -0.089(2×) -0.097(2×) -0.086(2×)	-0.087(8×)	-0.089(8×)
N_{amin}	-0.490(4×) -0.492(4×)	-0.497(6×) -0.495(2×)	-0.490(2×) -0.488(4×) -0.486(2×)	-0.503(8×)	-0.496(8×)
C_{met}	-0.418(16×)	-0.418(16×)	-0.418(16×)	-0.419(16×)	-0.418(16×)
Spin					
N_{py}	-	-	-0.050 -0.042(2×)	-	-0.049(4×)
N_{br}	-	-	-0.023 -0.050(2×) -0.040(2×)	-	-0.054(4×)
C_{α}			0.125(8×)		0.140(8×)
C_{β}			-0.007(8×)		-0.002(8×)
N_{amin}	-	-	0.004(4×) 0.003(4×)	-	0.002(8×)
C_{met}	-	-	0.000(16×)	-	0.000(16×)

2.1. Energetics

According to the Gibbs free energy data at room temperature (Table 1), the energies of the ^{m}[dmaphPcAg]^{q} complexes decrease upon reduction. However, even the structures of the [dmaphPcAg]$^{2-}$ complexes corresponding to the formal oxidation state Ag(0) seem to be stable. Except [dmaphPcAg]$^{+}$, the complexes in lower spin states are more stable. It implies that the ^{3}[dmaphPcAg]$^{+}$ biradical can be present in non-vanishing concentrations in the reaction system. Consequently, reactions (2) and (6) are correct. Despite the relative concentrations of the deexcitation products of the excited [dmaphPcAg]* and [dmaphPcAg…(MePh)$_2$I^{+}]* species not necessarily satisfy the Boltzmann distribution law, our results indicate that only ^{1}[dmaphPcAg]$^{-}$ and ^{3}[dmaphPcAg]$^{-}$ species can co-exist in comparable concentrations. In equilibria, the remaining ^{m}[dmaphPcAg]^{q} complexes

 doi:10.20944/preprints202402.0251.v1

with the same charges are present only in the more stable form because of the too large energy difference between their spin states. Therefore, if the LED@385 nm irradiation (corresponding to 310.7 kJ/mol energy) is fully absorbed by ^{2}[dmaphPcAg]^{0} excitation, the reaction (2) is shifted to the right in agreement with [23] (the reaction Gibbs energy of -26.5 kJ/mol at 298 K).

According to the data in Table 1, deprotonated [dmaphPcH$_n$]^{q} species, n = 2 or 1, seem to be more stable than their dehydrogenated counterparts (i.e., with q preserved). However, their relative stability is also dependent on the reactions of their formation. The reaction Gibbs energy of ^{2}Ag^{0} formation (with atomic Gibbs energy of -146.98864 Hartree) according to reaction (3) is highly positive (+235.0 kJ/mol for ^{3}[dmaphPcAg]$^{-}$ and +240.7 kJ/mol for ^{1}[dmaphPcAg]$^{-}$) and its equilibrium is shifted right due to subsequent formation and precipitation of Ag nanoparticles. Due to the lack of necessary data, we will not deal with the remaining (4) – (8) reaction equilibria.

2.2. Geometries

The DFT optimized geometries of the ^{m}[dmaphPcAg]^{q} complexes are very similar to the ^{2}[dmaphPcAg]^{0} structure presented in Fig. 1. Except for dimethylphenyl groups, all ^{m}[dmaphPcAg]^{q} structures are planar, only the central Ag atom might be slightly above the plane of four pyridine nitrogen atoms N_{py} (up to 0.019 Å in ^{3}[dmaphPcAg]$^{+}$, see Table 2). The values of the lengths of the Ag – N_{py} bonds, as well as of the N_{py} – Ag – N_{py} angles indicate that the C_4 symmetry axis is preserved in all the silver complexes except ^{4}[dmaphPcAg]^{0}, ^{1}[dmaphPcAg]$^{-}$, and ^{3}[dmaphPcAg]$^{-}$. The Ag – N_{py} bond lengths increase with complex reduction up to ^{1}[dmaphPcAg]$^{-}$ only. Therefore, the electron density transfer to Ag is not related to its out-of-plane movement.

The DFT optimized structures of ^{m}[dmaphPcH$_n$]^{q}, n = 2 → 0, are presented in Figs. 3, 5, 6, S1, S2 and in Table 3. Except for ^{1}[dmaphPcH]$^{-}$, their phthalocyanine cores are planar. Their H-N_{py} bond lengths increase during deprotonation/dehydrogenation of the central ring. Due to H-N_{py} bonds, the C_4 symmetry axis can be observed only in ^{2}[dmaphPc]$^{-}$ and ^{1}[dmaphPc]$^{2-}$.

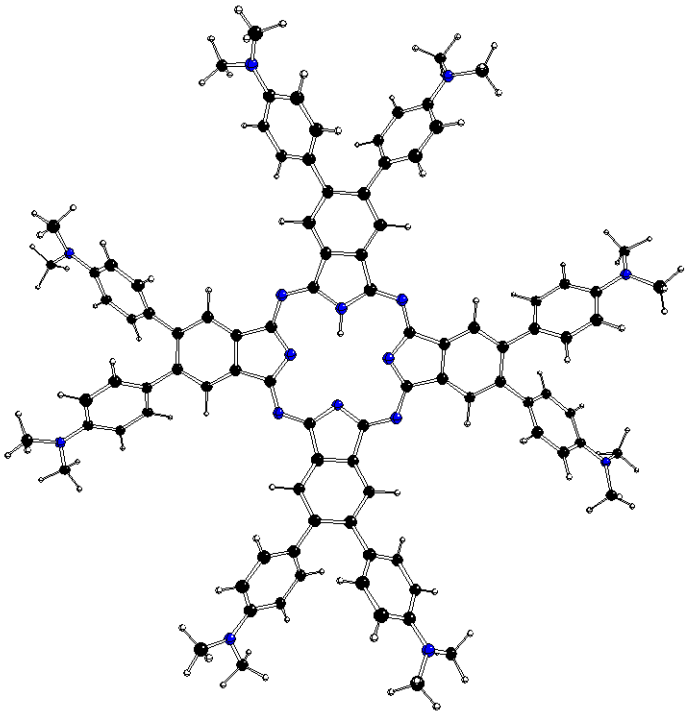

 doi:10.20944/preprints202402.0251.v1

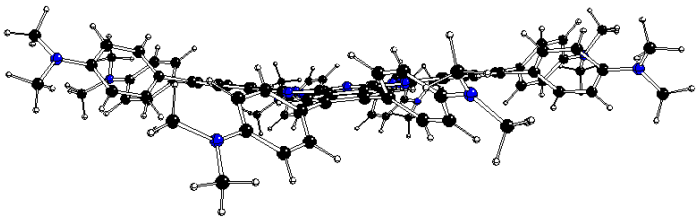

Figure 5. DFT optimized structure of ^{1}[dmaphPcH]$^{-}$ in $CHCl_3$ - above (top) and side (bottom) views (C – black, N – blue, H – white).

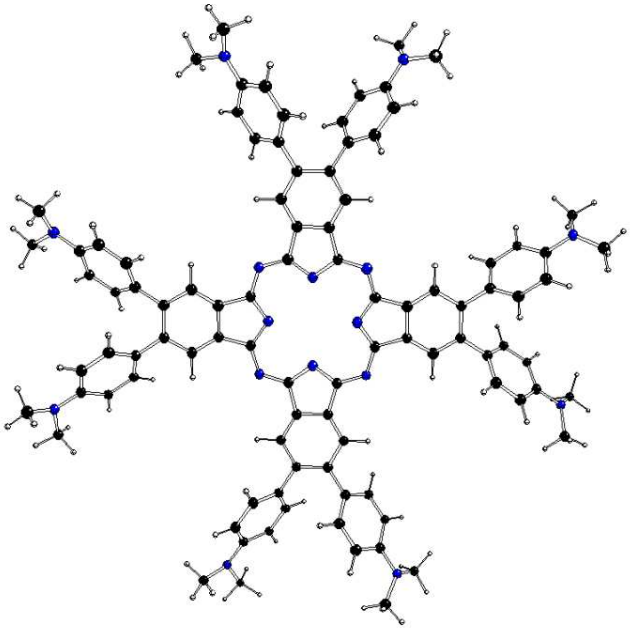

Figure 6. DFT optimized structure of ^{1}[dmaphPc]$^{2-}$ in $CHCl_3$ (C – black, N – blue, H – white).

2.3. Electronic Structure

The main features of the ^{m}[dmaphPcAg]^{q} complexes are presented in Figs. 7 – 9, S3 – S5 and Table 2. Their Ag – N_{py} bond orders and positive Ag charges decrease upon reduction up to [dmaphPcAg]$^{-}$. Except for complexes in singlet spin states, the d-electron populations of silver atoms are practically constant. The atomic charges of the pyrrole nitrogens N_{py} are more negative than that of the bridging nitrogens N_{br}, and the amine nitrogens N_{amin} have even less negative charges. During reduction of the complex, all N charges become even more negative. Positive charges of carbon atoms at the 4- and 7-positions of the isoindole units denoted as C_{α} decrease with reduction of the complex. Similarly, small negative charges of carbon atoms at isoindoles 5- and 6-positions denoted as C_{β} increase with reduction of the complex. Significantly more negative charges of the C_{met} methyl carbons do not depend on the charge q and spin state m of the ^{m}[dmaphPcAg]^{q} complexes. Only N_{amin} and C_{met} charges are not affected by the lower symmetry of the complexes studied.

The highest spin density at Ag atoms decreases only slightly with reduction. N_{py} atoms have ca two - three times lower spin density of the same sign, which rises with reduction. In both cases, the spin density increases with spin multiplicity. Except for ^{4}[dmaphPcAg]$^{2-}$, the spin density of opposite sign at N_{br} atoms is about one order lower and of variable signs. The spin density at C_{α} atoms is relevant only in anionic complexes and in higher spin states. C_{β} atoms have even lower spin density. The spin density at N_{amin} and C_{met} atoms is vanishing. Only the N_{br}, N_{amin} and C_{met} charges are not affected by the lower symmetry of the complexes under study. Except for ^{3}[dmaphPcAg]$^{+}$, only vanishing spin density can be found in dimethylaminophenyl groups.

 doi:10.20944/preprints202402.0251.v1

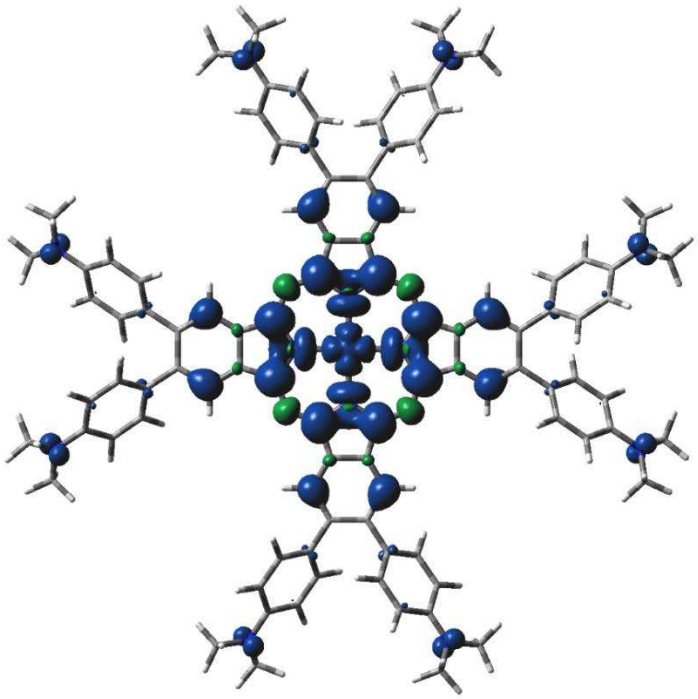

Figure 7. DFT calculated spin density of ^{3}[dmaphPcAg]$^{+}$ in $CHCl_3$ (0.001 a.u. isosurface).

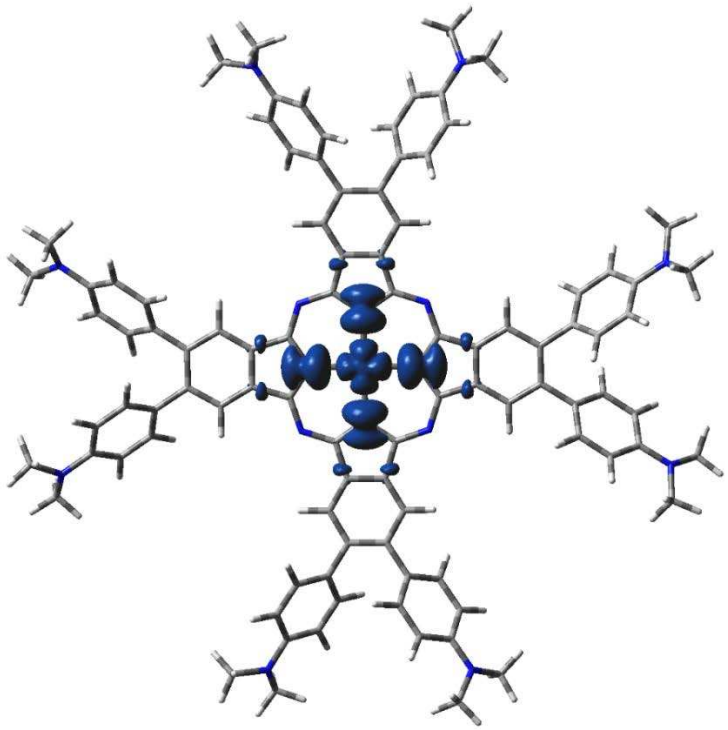

Figure 8. DFT calculated spin density of ^{2}[dmaphPcAg]^{0} in $CHCl_3$ (0.001 a.u. isosurface).

 doi:10.20944/preprints202402.0251.v1

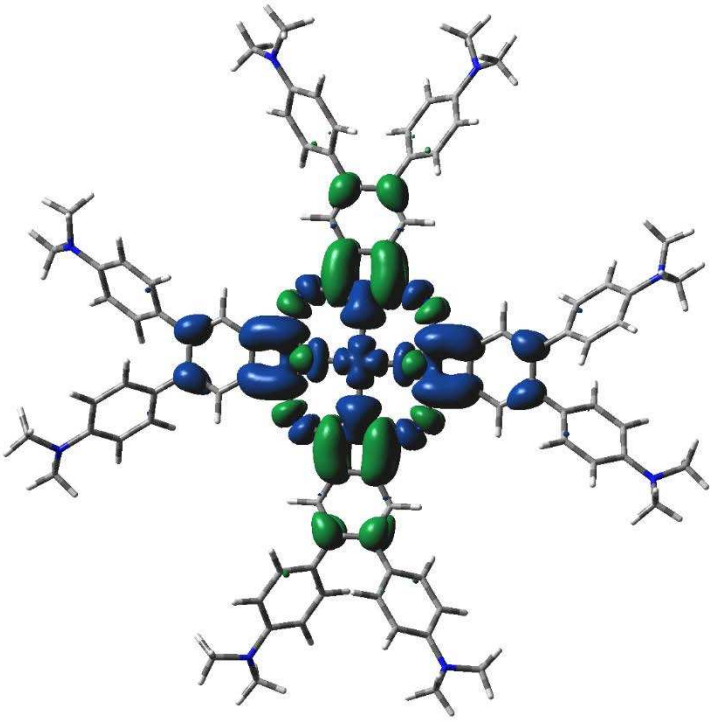

Figure 9. DFT calculated spin density of ^{2}[dmaphPcAg]$^{2-}$ in $CHCl_3$ (0.001 a.u. isosurface).

The main features of the ^{m}[dmaphPcH$_n$]^{q} species are presented in Figs. S6, S7, and Table 3. The H – N_{py} bond orders decrease with dehydrogenation/deprotonation. The same trend exhibits the most negative N_{py} charges, whereas the N_{br} ones exhibit a reverse trend. The even less negative N_{amin} charges increase with the negative charge of the whole species. The positive Cα charges decrease with the total charge of the species and increase with deprotonation/dehydrogenation. Only small changes in the very small C_{β} charges can be observed. Negative C_{met} charges are constant in all ^{m}[dmaphPcH$_n$]^{q} species under study and equal to those of ^{m}[dmaphPcAg]^{q}.

We have only two ^{2}[dmaphPcH$_n$]^{q} species with non-zero spin. The small spin densities at the N_{py} and N_{br} atoms are of the same sign, unlike the higher ones at C_{α} atoms. The vanishing spin density is at C_{β} and N_{amin} atoms. No spin density at C_{met} atoms can be observed.

2.4. Electron Transitions

In this section we will compare the TD-DFT calculated electron transitions of ^{m}[dmaphPcAg]^{q} complexes in $CHCl_3$ (Figures 10 – 13 and S8 – S11) with UV-vis spectra of in [dmaphPcAg]^{0} in $CHCl_3$ before (Figure 2) and during (Figure 4) photolysis.

 doi:10.20944/preprints202402.0251.v1

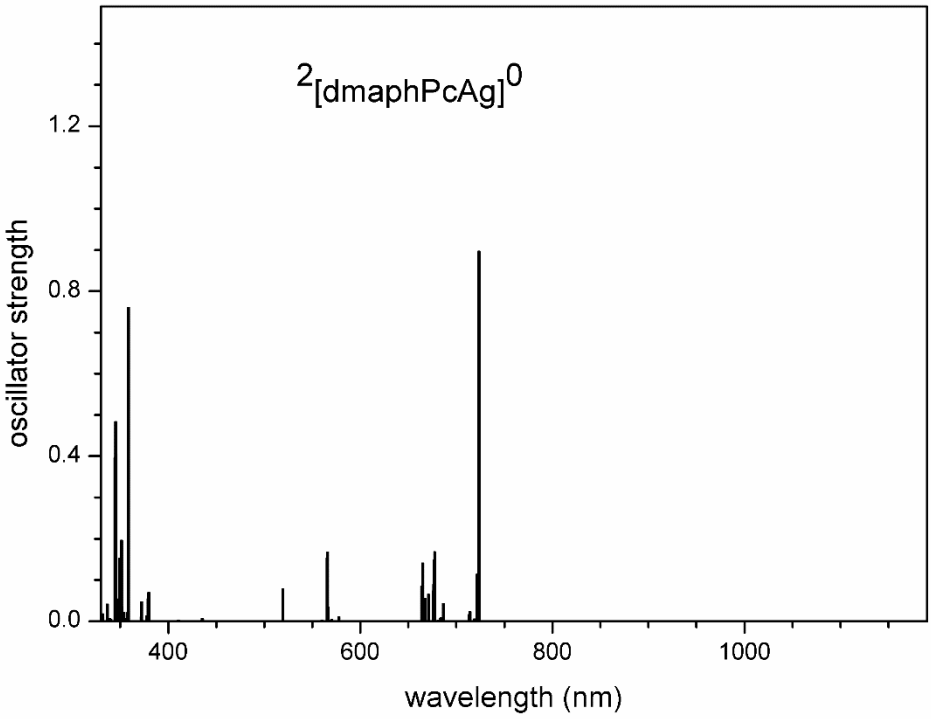

Figure 10. TD-DFT calculated electron transitions in ^{2}[dmaphPcAg]^{0} in $CHCl_3$.

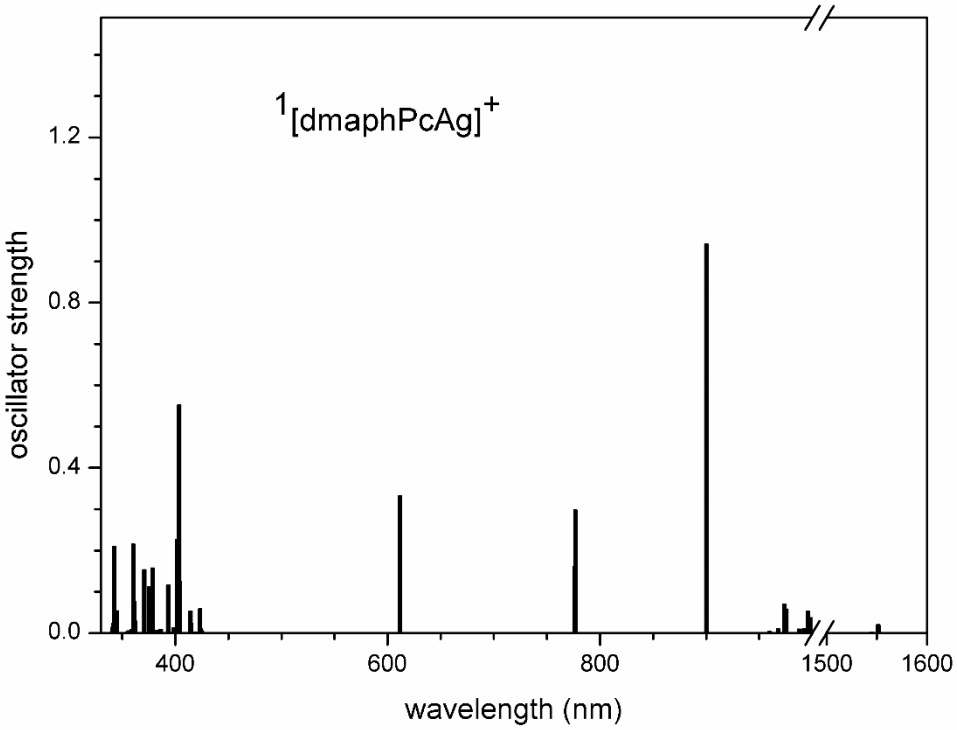

Figure 11. TD-DFT calculated electron transitions in ^{3}[dmaphPcAg]$^{+}$ in $CHCl_3$.

 doi:10.20944/preprints202402.0251.v1

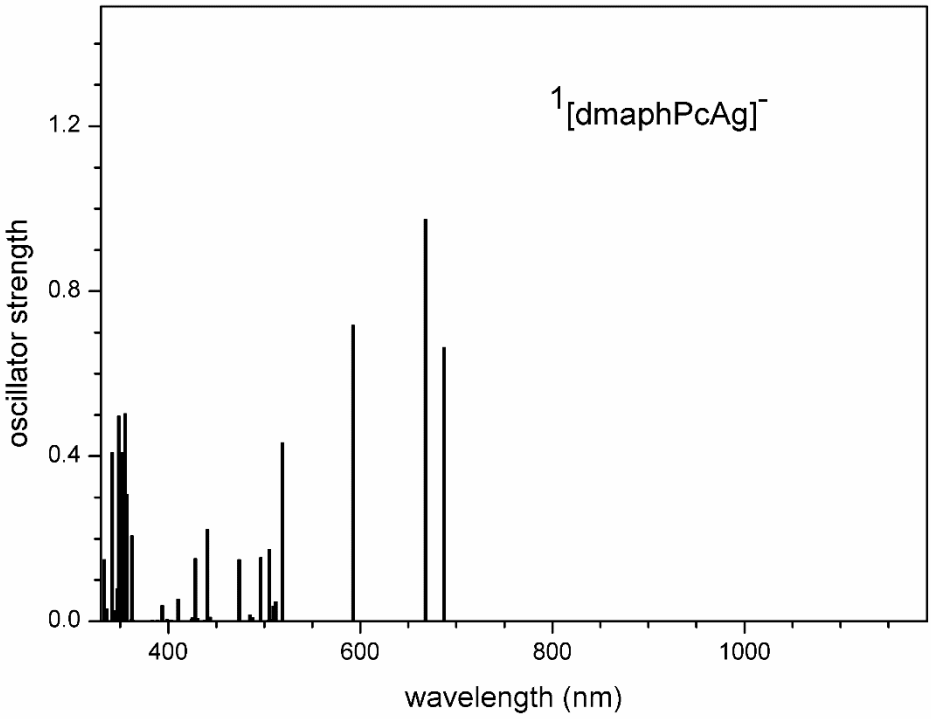

Figure 12. TD-DFT calculated electron transitions in ^{1}[dmaphPcAg]$^{-}$ in $CHCl_3$.

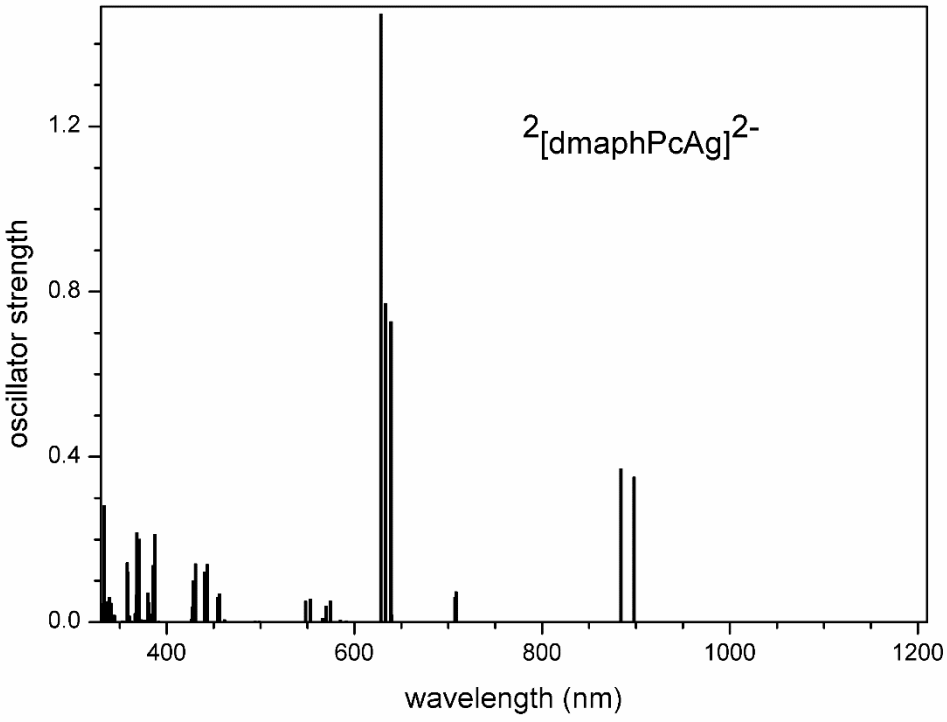

Figure 13. TD-DFT calculated electron transitions in ^{2}[dmaphPcAg]$^{2-}$ in $CHCl_3$.

 doi:10.20944/preprints202402.0251.v1

Very intense TD-DFT electron transitions of ^{2}[dmaphPcAg]^{0} at 723 and 724 nm (Fig. 10) can be assigned rather to the 730 nm shoulder than to the 700 nm peak in experimental spectra (Fig. 2). Similarly, the intense electron transitions at 359 nm correspond more probably to the experimental peak at 360 nm than at 300 nm. It implies the existence of several species in the solution.

Intense electron transitions of ^{3}[dmaphPcAg]$^{+}$ calculated at 2390 nm, as well as less intense ones at 915 and 856 nm (Fig. 11) are not observed in the experimental spectra of the reaction system in Fig. 4. This excludes its presence at measurable concentrations. The same holds for ^{1}[dmaphPcAg]$^{+}$ due to the very intense TD-DFT electron transition at 900 nm (Fig. S8), which is absent in the experimental spectra (Fig. 4). Analogously, the calculated relevant electron transitions of ^{4}[dmaphPcAg]^{0} at 1276 and 1210 nm (Fig. S9) missing in experimental spectra are in contradiction with the presence of this species in the reaction system (Fig. 4).

On the other hand, the experimental peak at 680 nm can be assigned to an intense electron transition at 687 nm and the 660 nm peak to an intense 668 nm transition whereas the 593 nm electron transition might correspond to its shoulder. This supports the presence of ^{1}[dmaphPcAg]$^{-}$ in the reaction system (Figs. 4 and 12). The presence of ^{3}[dmaphPcAg]$^{-}$ in the reaction system cannot be excluded because the experimental peak at 730 nm (Fig. 4) can be explained as the very intense TD-DFT electron transition at 724 nm and the very intense electron transition at 619 nm (Fig. S10) can be superimposed by the scarcely visible shoulder of the very intense peak at 700 nm.

The absence of ^{2}[dmaphPcAg]$^{2-}$ in the reaction system is due to the missing experimental peaks corresponding to the relevant electron transitions at 898 nm and 884 nm (Figs. 4 and 13). Analogously, the absence of experimental peaks corresponding to the TD-DFT electron transitions of ^{4}[dmaphPcAg]$^{2-}$ at 1153 nm and 812 nm (Figs. 4 and S11) is the reason for the exclusion of this species from the reaction system.

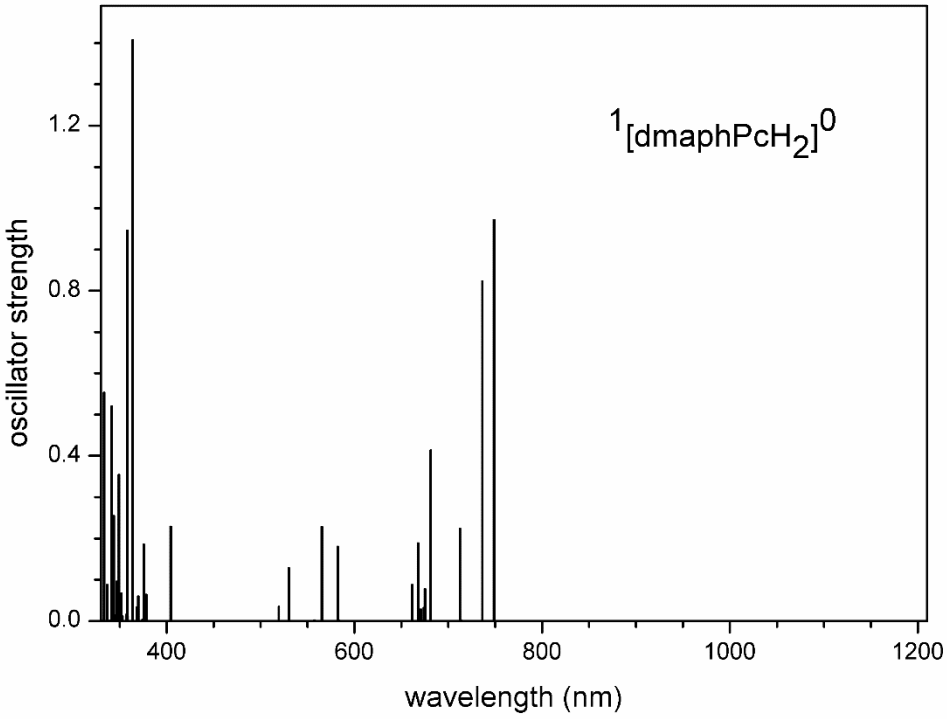

Figure 14. TD-DFT calculated electron transitions in ^{1}[dmaphPcH$_2$]^{0} in CHCl$_3$.

 doi:10.20944/preprints202402.0251.v1

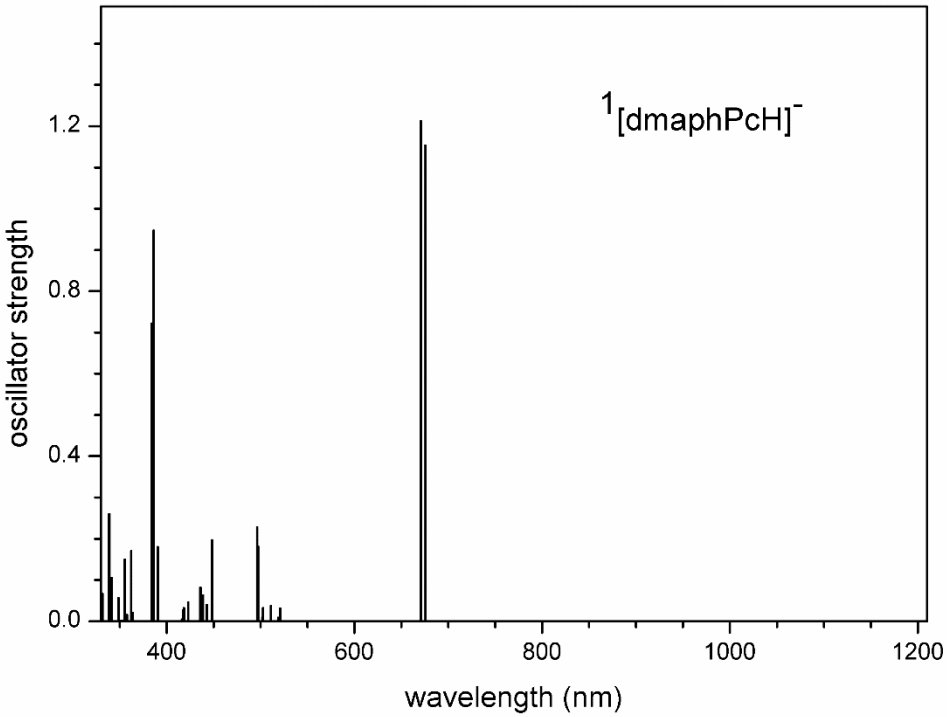

Figure 15. TD-DFT calculated electron transitions in ^{1}[dmaphPcH]$^-$ in $CHCl_3$.

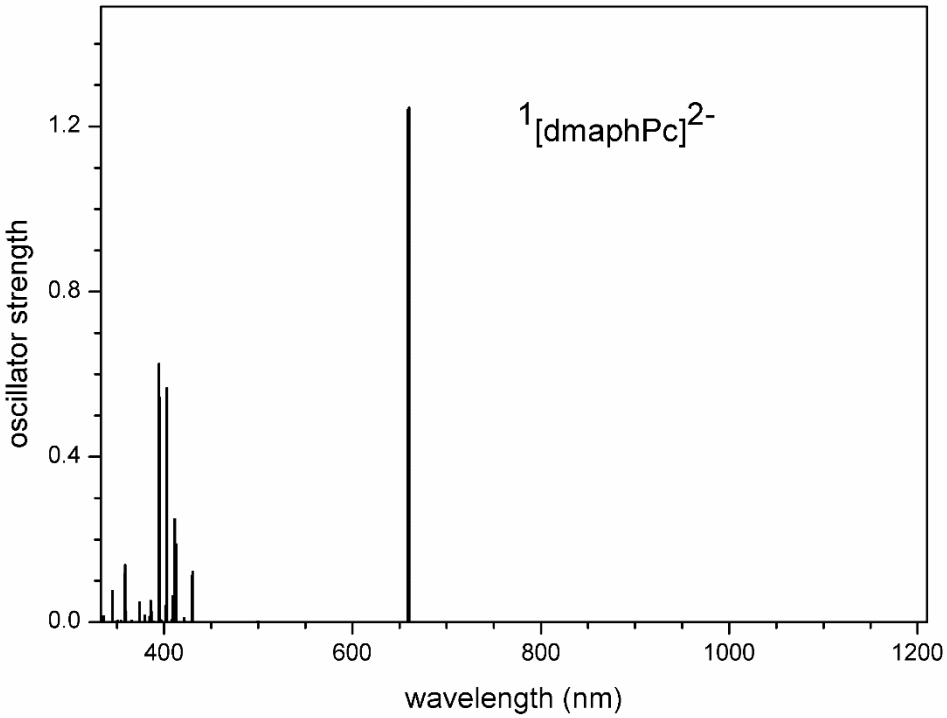

Figure 16. TD-DFT calculated electron transitions in ^{1}[dmaphPc]$^{2-}$ in $CHCl_3$.

 doi:10.20944/preprints202402.0251.v1

Very intense TD-DFT electron transitions of ^{1}[dmaphPcH$_2$]^{0} at 736 and 749 nm (Fig. 14) can be assigned to the 750 nm peak in the experimental spectra (Fig. 2). Similarly, the experimental peak at 340 nm can be explained by the calculated electron transitions at 358 nm and 364 nm. Therefore, the agreement between the experimental and calculated spectral parameters is worse than in the case of ^{2}[dmaphPcAg]^{0}.

Very intense TD-DFT electron transitions of ^{1}[dmaphPcH]$^{-}$ at 675 nm and 671 nm (Fig. 15) can be assigned to the experimental peak at 680 nm (Fig. 4). The experimental peak at 380 nm can be explained by the very intense calculated electron transitions at 386 and 384 nm. Its neutral analogue ^{2}[dmaphPcH]^{0} can be excluded from the reaction system due to missing experimental peaks corresponding to TD-DFT electron transitions at 1183 nm, 1154 nm, 832 nm, and 788 nm (Figs. 4 and S12).

The very intense calculated electron transitions of ^{1}[dmaphPc]$^{2-}$ at 660 nm and 658 nm (Fig. 16) can be assigned to the 660 nm or 680 nm shoulder (but not to both) of the 730 nm peak shoulder in the reaction spectra (Fig. 4). TD-DFT electron transitions of ^{2}[dmaphPc]$^{-}$ at 778 nm and 777 nm (Fig. S13) can also be superimposed by the intense 730 nm peak shoulder of the reaction system (Fig. 4) and this peak can be assigned to very intense 722 nm and 721 nm electron transitions, too.

We can conclude that our TD-DFT interpretation of the experimental UV-vis spectra indicates that the ^{2}[dmaphPcAg]^{0}, ^{1}[dmaphPcAg]$^{-}$, ^{3}[dmaphPcAg]$^{-}$, ^{1}[dmaphPcH$_2$]^{0}, ^{1}[dmaphPcH]$^{-}$, ^{2}[dmaphPc]$^{-}$, and ^{1}[dmaphPc]$^{2-}$ species can be present in the reaction system under study.

3. Discussion

Two- or even three-electron reduction of the ^{3}[dmaphPc]$^{+}$ species causes only small changes in the electron and spin population at the central Ag atom, and the same holds for the Ag-N$_{py}$ bond. The added electrons are prevailingly distributed on the dmaphPc^{2-} ligand only which is typical for 'non-innocent' ligands. This reduction does not cause a shift of Ag from the phthalocyanine plane. However, neutral Ag nanoparticles should be formed within the endothermic reaction (3) which is connected with ca. 0.8 electron addition to Ag simultaneously with its move from the ligand plane. The planarity of the phthalocyanine core of ^{2}[dmaphPc]$^{-}$ is preserved. These changes should proceed in several reaction steps including the aggregation of the [dmaphPcAg]$^{-}$ species in the solution. However, this does not coincide with its negative charge.

The results of our 'broken symmetry' DFT calculations indicate the nonexistence of singlet biradicals. According to the energy data, the ^{3}[dmaphPcAg]$^{+}$ concentration should dominate over their singlet counterparts, but the UV-vis spectra [23] do not confirm its presence in reaction systems. Based on EPR measurements using spin traps [23], this can be explained by the very low stability of ^{3}[dmaphPcAg]$^{+}$. Moreover, only this species has non-vanishing spin density at N$_{amin}$ atoms (see Fig. 7) as supposed in [23]. The calculated electron transitions of the EPR silent ^{1}[dmaphPcAg]$^{+}$ species do not agree with UV-vis spectra [23] and so it is not present in reaction solutions.

The presence of ^{2}[dmaphPcAg]^{0} in reaction solutions is in agreement with the DFT and TD-DFT calculations as well as with the EPR and UV-vis measurements [23]. However, the calculated electron transitions cannot explain all the spectral peaks in Fig. 2. This indicates the presence of other species in the CHCl$_3$ solution of ^{2}[dmaphPcAg]^{0}. The comparison of UV-vis spectra with the TD-DFT electron transition as well as the DFT energy data indicate the absence of ^{4}[dmaphPcAg]^{0} in reaction solutions.

The coexistence of ^{1}[dmaphPcAg]$^{-}$ and ^{3}[dmaphPcAg]$^{-}$ in reaction solutions is allowed by their energies and by the agreement of the calculated electron transitions with UV-vis spectra [23]. ^{1}[dmaphPcAg]$^{-}$ is EPR silent.

Energy data indicate that the concentration of ^{2}[dmaphPcAg]$^{2-}$ should dominate over ^{4}[dmaphPcAg]$^{2-}$ but the calculated electron transitions of both species do not agree with UV-vis spectra [23], implying their absence in reaction solutions.

Based on TD-DFT electron transitions and UV-vis spectra [23], the EPR silent ^{1}[dmaphPcH$_2$]^{0} species and its deprotonated products ^{1}[dmaphPc]$^{-}$ and ^{1}[dmaphPc]$^{2-}$ can be present in reaction solutions. The same holds for the dehydrogenated product ^{2}[dmaphPc]$^{-}$ but not for ^{2}[dmaphPcH]^{0}.

 doi:10.20944/preprints202402.0251.v1

4. Methods

Standard B3LYP [26] geometry optimization with Grimme's GD3 dispersion correction [27] of ^{m}[dmaphPcAg]^{q}, q = -2 to +1, in two lowest spin states m, and ^{m}[dmaphPcH$_n$]^{q} , n = 2 to 0, q = 0, 1, or 2, in the lowest spin states m, in $CHCl_3$ solutions using the cc-pVDZ-PP pseudopotential and basis set for Ag [28] and cc-pVDZ basis sets for the remaining atoms [29] was performed. All calculations were carried out using an unrestricted formalism within 'broken symmetry' treatment [25]. Solvent effects were approximated by the SMD (Solvation Model based on solute electron Density) modification [30] of the integral equation formalism polarizable continuum model. The optimized structures were tested on the absence of imaginary vibrations by vibrational analysis. The excited state energies and the intensities of the corresponding electron transitions were evaluated using the time-dependent DFT method (TD-DFT) [31] for 90 - 120 states. The electronic structure was evaluated in terms of Natural Bond Orbital (NBO) population analysis [32]. All calculations were performed using the Gaussian16 [33] program package.

5. Conclusions

This study aims to supplement the quantum-chemical studies related to the [dmaphPcAg] photoinitiator of polymerization reactions in [23]. We tested the initial steps (1) – (3) of FRP proposed in [23] by (TD-)DFT interpretation of the EPR and UV-vis measurements by testing the presence of possible reaction intermediates ^{m}[dmaphPcAg]^{q}, q = 1 → -2, ^{1}[dmaphPcH$_2$]^{0}, and its deprotonation/dehydrogenation products.

Our results suggest the presence of crucial unstable ^{3}[dmaphPcAg]$^{+}$ species which was deduced by EPR spin trap experiments [23], but its identification was complicated due to the presence of other similar compounds in reaction solutions.

In addition to ^{2}[dmaphPcAg]^{0}, our results suggest the coexistence of both ^{1}[dmaphPcAg]$^{-}$ (EPR silent) and ^{3}[dmaphPcAg]$^{-}$ species in reaction solutions as well. Therefore, the supposed intermediates of the reactions (1) – (3) can be identified. The presence of the EPR silent species ^{1}[dmaphPcH$_2$]^{0}, ^{1}[dmaphPc]$^{-}$ and ^{1}[dmaphPc]$^{2-}$ as well as of the radical ^{2}[dmaphPc]$^{-}$ in reaction solutions cannot be excluded.

However, the formation of Ag nanoparticles by reaction (3) may be a weak point of the proposed reaction mechanism from the energetic, stereochemistry, and electronic structure points of view. Unfortunately, we do not have sufficient information to propose any alternative reaction mechanisms. Further experimental and theoretical studies are desirable in this field.

Supplementary Materials: The following supporting information can be downloaded at: www.mdpi.com/xxx/s1, Figures S1 – S2. DFT optimized structures of ^{2}[dmaphPcH]^{0} and ^{2}[dmaphPc]$^{-}$ in $CHCl_3$. Figures S3 – S7. DFT calculated spin density of ^{4}[dmaphPcAg]^{0}, ^{3}[dmaphPcAg]$^{-}$, ^{4}[dmaphPcAg]$^{2-}$, ^{2}[dmaphPcH]^{0}, and ^{2}[dmaphPc]$^{-}$ in $CHCl_3$. Figures S8 – S13. TD-DFT calculated electron transitions in ^{1}[dmaphPcAg]$^{+}$, ^{4}[dmaphPcAg]^{0}, ^{3}[dmaphPcAg]$^{-}$, ^{4}[dmaphPcAg]$^{2-}$, ^{2}[dmaphPcH]^{0}, and ^{2}[dmaphPc]$^{-}$ in $CHCl_3$.

Funding: This research has been supported by the Slovak Research and Development Agency (project no. APVV-19-0087), by the Slovak Scientific Grant Agency VEGA (project no. 1/0175/23), and by Ministry of Education, Science, Research and Sport of the Slovak Republic within the scheme "Excellent research teams". The author thanks the HPC center at the Slovak University of Technology in Bratislava, which is a part of the Slovak Infrastructure of High Performance Computing (SIVVP project ITMS 26230120002, funded by European Region Development Funds) for the computational time and resources made available.

Institutional Review Board Statement: Not applicable.

Informed Consent Statement: Not applicable.

Data Availability Statement: Data are contained within the article or supplementary material.

Conflicts of Interest: The funders had no role in the design of the study; in the collection, analyses, or interpretation of data; in the writing of the manuscript; or in the decision to publish the results.

References

1. Urbani, M.; Ragoussi, M.-E.; Nazeeruddin, M. K.; Torres, T. Phthalocyanines for dye-sensitized solar cells. *Coord. Chem. Rev.* **2019,** *381*, 1-64.
2. Kaliya, O. L.; Lukyanets, E. A.; Vorozhtsov, G. N. Catalysis and Photocatalysis by Phthalocyanines for Technology, Ecology, and Medicine. *J. Porphyrins Phthalocyanines* **1999**, *3*, 592−610.
3. Sorokin, A. B. Phthalocyanine Metal Complexes in Catalysis. *Chem. Rev.* **2013**, *113*, 8152−8191.
4. Juzenas, P. Lasers in Therapy of Human Diseases. *Trends Cancer Res*. **2005,** *1*, 93−110.
5. O'Riordan, K.; Akilov, O. E.; Hasan, T. The Potential for Photodynamic Therapy in the Treatment of Localized Infections. *Photodiagn. Photodyn. Ther*. **2005**, *2*, 247−262.
6. Sekkat, N.; van den Bergh, H.; Nyokong, T.; Lange, N. Like a Bolt from the Blue: Phthalocyanines in Biomedical Optics. *Molecules* **2012**, *17*, 98−144.
7. Allen, C. M.; Sharman, W. M.; Van Lier, J. E. Current Status of Phthalocyanines in the Photodynamic Therapy of Cancer. *J. Porphyrins Phthalocyanines* **2001**, *5*, 161−169.
8. Lukyanets, E. A. Phthalocyanines as Photosensitizers in the Photodynamic Therapy of Cancer. *J. Porphyrins Phthalocyanines* **1999**, *3*, 424−432.
9. da Silva, R. N.; Cunha, A.; Tomé, A. C. Phthalocyaninesulfonamide Conjugates: Synthesis and Photodynamic Inactivation of Gram-negative and Gram-positive Bacteria. *Eur. J. Med. Chem*. **2018**, *154*, 60−67.
10. Elemans, J. A. A. W.; van Hameren, R.; Nolte, R. J. M.; Rowan, A. E. Molecular Materials by Self-assembly of Porphyrins, Phthalocyanines, and Perylenes. *Adv. Mater*. **2006**, *18*, 1251−1266.
11. Gsaenger, M.; Bialas, D.; Huang, L.; Stolte, M.; Wuerthner, F. Organic Semiconductors Based on Dyes and Color Pigments. *Adv. Mater*. **2016**, *28*, 3615−3645.
12. Ndiaye, A. L.; Delile, S.; Brunet, J.; Varenne, C.; Pauly, A. Electrochemical Sensors Based on Screen-printed Electrodes: The Use of Phthalocyanine Derivatives for Application in VFA Detection. *Biosensors-Ba*sel **2016**, *6*, 0046.
13. Liang, Y.; Lv, W.; Luo, X.; He, L.; Xu, K.; Zhao, F.; Huang, F.; Lu, F.; Peng, Y. A Comprehensive Investigation of Organic Active Layer Structures Toward High Performance Near-infrared Phototransistors. *Synth. Met*. **2018**, *240*, 44−51.
14. Woehrle, D.; Schnurpfeil, G.; Makarov, S. G.; Kazarin, A.; Suvorova, O. N. Practical Applications of Phthalocyanines – from Dyes and Pigments to Materials for Optical, Electronic and Photoelectronic Devices. M*akrogeterotsikly* **2012**, *5*, 191−202.
15. de la Torre, G.; Vazquez, P.; Agullo-Lopez, F.; Torres, T. Phthalocyanines and Related Compounds: Organic Targets for Nonlinear Optical Applications. *J. Mater. Chem*. **1998**, *8*, 1671−1683.
16. Chen, Y.; Hanack, M.; Blau, W. J.; Dini, D.; Liu, Y.; Lin, Y.; Bai, J. Soluble Axially Substituted Phthalocyanines: Synthesis and Nonlinear Optical Response. *J. Mater. Sci.* **2006**, *41*, 2169−2185.
17. Wrobel, D.; Dudkowiak, A. Porphyrins and Phthalocyanines − Functional Molecular Materials for Optoelectronics and Medicine. *Mol. Cryst. Liq. Cryst*. **2006**, *448*, 15−38.
18. Wu, Z.; Jung, K.; Boyer, C. Effective Utilization of NIR Wavelengths for Photo-Controlled Polymerization: Penetration Through Thick Barriers and Parallel Solar Syntheses. *Angew. Chem*. **2020**, *59*, 2013–2017.
19. Corrigan, N.; Xu, J.; Boyer, C. A Photoinitiation System for Conventional and Controlled Radical Polymerization at Visible and NIR Wavelengths. *Macromolecules* **2016**, *49*, 3274–3285.
20. Korkut, S. E.; Temel, G.; Balta, D. K.; Arsu, N.; Şener, M. K. Type II photoinitiator substituted zinc phthalocyanine: Synthesis, photophysical and photopolymerization studies. *J. Lumin*. **2013**, *136*, 389–394.
21. Breloy, L.; Brezová, V.; Blacha-Grzechnik, A.; Presset, M.; Yildirim, M. S.; Yilmaz, I.; Yagci, Y.; Versace, D.-L. Visible Light Anthraquinone Functional Phthalocyanine Photoinitiator for Free-Radical and Cationic Polymerizations. *Macromolecules* **2020**, *53*, 112–124.
22. Wang, Y.; Han, B.; Shi, R.; Pan, L.; Zhang, H.; Shen, Y.; Li, C.; Huang, F.; Xie, A. Preparation and characterization of a novel hybrid hydrogel shell for localized photodynamic therapy. *J. Mater. Chem. B* **2013**, *1*, 6411–6417.
23. Breloy, L.; Alcay, Y.; Yilmaz, I.; Breza, M., Bourgon, J.; Brezová, V.; Yagci, Y., Versace, D.-L. Dimethyl amino phenyl substituted silver phthalocyanine as a UV- and visible-light absorbing photoinitiator: in situ preparation of silver/polymer nanocomposites. *Polym. Chem*. **2021**, *12*, 1273-1285.
24. Breza, M. On the Jahn–Teller Effect in Silver Complexes of Dimethyl Amino Phenyl Substituted Phthalocyanine. *Molecules* **2023**, *28*, 7019.
25. Noodleman, L. Valence bond description of antiferromagnetic coupling in transition metal dimer. *J. Chem. Phys*. **1981**, *74*, 5737-5743.
26. Becke, A. D. Density-functional thermochemistry. III. The role of exact exchange. *J. Chem. Phys*. **1993**, *98*, 5648-5652.

 doi:10.20944/preprints202402.0251.v1

27. Grimme, S.; Antony, J.; Ehrlich, S.; Krieg, H. A consistent and accurate ab initio parameterization of density functional dispersion correction (DFT-D) for the 94 elements H-Pu. *J. Chem. Phys*. **2010**, *132*, 154104.
28. Pritchard, B.P.; Altarawy, D.; Didier, B.; Gibson, T.D.;Windus, T.L. New Basis Set Exchange: An Open, Up-to-Date Resource for the Molecular Sciences Community. *J. Chem. Inf. Model*. **2019**, *59*, 4814–4820.
29. Dunning, T.H., Jr. Gaussian basis sets for use in correlated molecular calculations. I. The atoms boron through neon and hydrogen. *J. Chem. Phys*. **1989**, *90*, 1007–1023.
30. Marenich, A.; Cramer, C.; Truhlar, D. Universal Solvation Model Based on Solute Electron Density and on a Continuum Model of the Solvent Defined by the Bulk Dielectric Constant and Atomic Surface Tensions. *J. Phys. Chem. B* **2009**, *113*, 6378– 6396.
31. Bauernschmitt, R.; Ahlrichs, R. Treatment of electronic excitations within the adiabatic approximation of time dependent density functional theory. *Chem. Phys. Lett*. **1996**, *256*, 454–464.
32. Foster, J. P.; Weinhold, F. Natural Hybrid Orbitals. J. *Am. Chem. Soc.* **1980**, *102*, 7211-7218.
33. Frisch, M.J.; Trucks, G.W.; Schlegel, H.B.; Scuseria, G.E.; Robb, M.A.; Cheeseman, J.R.; Scalmani, G.; Barone, V.; Petersson, G.A.; Nakatsuji, H.; et al. *Gaussian 16, Revision B.01*; Gaussian, Inc.: Wallingford, CT, USA, 2016.